Application Of MEMS In Deformation Monitoring Of Model Foundation Pit

Di Wu[1], Yang Yi[1], Wenbo Lin[1], Jianjian Wu[1], and Yanxin Yang[2*]

[1] School of Architecture and Transportation Engineering, Guilin University of Electronic Technology, Guilin, Guangxi 541004, P.R. China
[2] School of Civil Engineering, Sichuan University of Science & Engineering, Zigong, Sichuan 643000, P.R. China
[*] Corresponding author. E-mail: yanxinyangswjtu@foxmail.com

Received: Jan. 01, 2023; Accepted: Sept. 11, 2023

Real-time monitoring of foundation pits is an important part of the engineering construction. This paper proposes a method of deformation monitoring of foundation pit based on MEMS technology. The algorithm based on time-domain integration is adopted, and a fixed distance test is designed to verify the feasibility of the algorithm. Through the indoor model test of foundation pit monitoring, MEMS sensors are embedded to collect the acceleration, rotation angle and the other signals of soil movement, and then the acceleration signal is integrated to obtain displacement by algorithm calculation. Finally, the deformation characteristics of soil in the process of foundation pit are analyzed by using soil displacement and rotation angle to investigate the effectiveness of applying MEMS technology to foundation pit monitoring. The test results show that the MEMS sensor could accurately collect the acceleration, rotation angle and other signals of soil movement in model box. The monitoring method proposed in this paper lay a theoretical foundation and experimental verification for the application of MEMS technology in foundation pit monitoring.

Keywords: MEMS technology, excavation deformation monitoring, Acceleration, Time domain integration algorithm, Displacement of soil

http://dx.doi.org/10.6180/jase.202410_27(10).0015

1. Introduction

In recent years, with the rapid development of urban construction in China, the underground space has been highly valued and used in huge quantities to satisfy the needs of urban development, leading to a significant number of foundation pit projects.

Foundation pit engineering is mostly located in the downtown area, with dense building distribution, limited construction sites, complex construction environment and high-security requirements [1], due to the complexity of soil formation and the imperfection of foundation pit design theory, there is a significant discrepancy between the theoretical calculation of soil displacement and the real situation, and it is impossible to comprehensively predict the actual deformation state of foundation pit soil [2]. Therefore, it is crucial to pay attention to the soil movement of foundation pit during the entire excavation to ensure construction safety. Foundation pit monitoring refers to the observation and analysis of geotechnical aspects of the foundation pit, including the displacement of the supporting structure and soil, and changes in the surrounding environmental conditions during foundation pit excavation or underground engineering construction, as well as the assessment of the impact of the construction on the surrounding environment based on the prediction, and the timely feedback of the monitoring results.

The traditional monitoring techniques are mostly based on portable inclinometers, fixed inclinometers, total stations, GPS, 3D laser scanners and the other monitoring methods. The fixed inclinometer can measure the horizontal displacement of the soil. However, this it is limited by the zero-bias error of the instrument [3], and the

measurement of horizontal displacement depends on the zero-displacement reference point. The inclinometer may be affected by shock and other conditions in use, which may result in systematic errors. Zero displacement are required in practical engineering to ensure the accuracy of measurement data [4]. The total station monitoring is to set a relatively stable reference point close to the foundation pit first, and then to monitor the horizontal displacement of the foundation pit under the condition based on the monitoring point and the reference point. While the actual construction environment of the foundation pit is complex, it is difficult to ensure the general view condition, and serious station setting error and back-view error will occur if the total station is not used properly [5]. Although GPS can rapidly obtain soil deformation data, its vertical measurement accuracy is low and its ability to monitor soil deformation is limited [6–8]. The constraint of the point-for-surface monitoring method can be overcome by using equipment to monitor the soil surface using three-dimensional laser scanning technology [9]. However, the widespread use of this technology in actual engineering is constrained due to its expensive cost and complex operation [10, 11]. The portable inclinometer is a popular tool for monitoring foundation pit deformation in China compared to earlier techniques because of its high accuracy, affordability, flexibility, and convenience. However, it has some obvious drawbacks, including the fact that it is point-to-surface monitoring and relies too heavily on manual operation.

In summary, the fixed inclinometer is limited by the zero-bias error of the instrument, and the horizontal displacement measurement depends on the zero-displacement reference point. The total station is affected by the actual construction environment, so it is difficult to ensure the general view condition [5]. The accuracy of GPS vertical measurement is low and the monitoring ability of soil deformation is limited [6-8]. Due to the high cost and complex operation, the application of 3D laser scanning technology in practical engineering is limited [10, 11]. The portable clinometer also has some obvious disadvantages, including that it is point-to-point monitoring and relies too heavily on manual operation. The above monitoring methods may have some disadvantages to some extent.

In recent years, there has been a lot of research done to improve the intelligence level and precision of foundation pit deformation monitoring technology. Among them, optical fiber sensors are a type of sensing technology that has recently advanced quickly. Distributed optical fiber sensors can be used for remote distributed monitoring and have excellent endurance, high precision, and small size. Related researchers use fiber Bragg grating technology to track the horizontal displacement of excavations, to assess the viability of using fiber optic technology to track foundation pit deformation [12], and other purposes. However, it is challenging to implement this technique on a broad scale due to the limitations of the high cost of the demodulator and laying line, and the lack of real-time monitoring [13]. Additionally, methods like unmanned aerial vehicle images [14], ultrasonic wave [15], dense surface modeling technology [16] and ground-based SAR (Synthetic Aperture Radar) micro-deformation monitoring [17] have also been used to monitor the deformation of foundation pits.

In addition, MEMS (Micro Electro Mechanical Systems) sensing technology based on Micro-machining and Micro-processing technology is also been applied to detection due to its advantages of integration, miniaturization, low energy consumption, low cost, and high accuracy. For example, the microsensor technology can be used to identify the initiation time of impact induced elastic waves [18], which takes advantage of the small size of MEMS to produce an impact ball with sensors for impact testing to verify its feasibility. MEMS technology can be used under appropriate protection and in suitable soil environments, and actual engineering has been analyzed using MEMS technology to monitor data [19]. For example, Li et al. [20] propose a technical method for real-time monitoring of reservoir bank slope deformation using MEMS inertial sensors, comprehensively observing the three-dimensional motion state of slope deformation. Ha D. W. developed a wireless drilling inclinometer system based on MEMS, and verified the applicability and data reliability of the developed wireless MEMS drilling inclinometer through on-site testing [21]. There are also applications in foundation pits monitoring, such as in-place inclinometers based on microelectron mechanical systems technology [22], wireless shape accelerated array system which has used for real-time construction monitoring [23], and the geotechnical monitoring had been conducted by MEMS sensor [24]. However, MEMS sensors do not obtain a displacement signal that directly represents the deformation of the soil mass, instead, they gather and analyze signals of soil deformation acceleration and rotation angle.

This research proposes a foundation pit deformation monitoring method based on MEMS technology based on the current state of development of foundation pit deformation monitoring technology. First, a time domain integral-based acceleration signal rotation displacement algorithm is provided, and a fixed-distance test is created to confirm the accuracy and correctness of the algorithm. The foundation pit deformation monitoring interior model test is

then completed. MEMS sensors are buried in the ground to gather the rotation and acceleration signals of soil deformation movement. An algorithm is then used to calculate the acceleration signal into the appropriate displacement signal. Finally, the viability of using MEMS technology to monitor the deformation of the foundation pit is examined using the soil displacement and rotation angle signals to study the deformation of the soil during excavation.

2. Mems acceleration signal shift algorithm

When tracking the soil deformation in the excavation, MEMS technology cannot directly receive the displacement signal. Instead, the acceleration signal caused by soil deformation motion is collected by the MEMS sensor, and the integral algorithm subsequently converts the acceleration signal into the corresponding displacement signal. Time-domain integration and frequency-domain integration are the two most popular techniques for integrating acceleration signals [25]. The displacement signal is solved using the time-domain integration method in this paper.

The workflow of acceleration signal integration algorithm is depicted in Fig. 1. The preprocessing steps for the collected source acceleration signal are zero-bias correction and trend term elimination [26], followed by integration. The preprocessed acceleration signal is then used to calculate the displacement signal and the integral energy. Finally, the energy correction of displacement energy is carried out to produce a more precise displacement.

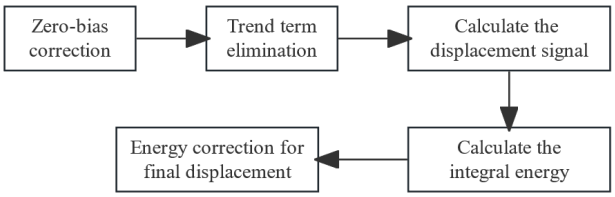

Fig. 1. Acceleration signal integration algorithm flow

2.1. Acceleration signal preprocessing

(1) Zero-bias correction

In the ideal state, when the three-axis MEMS sensor is at a static state and the Z-axis is perpendicular to the horizontal plane, the acceleration signal output values corresponding to the three axes of X, Y and Z satisfy $a_x = 0, a_y = 0, a_z = g$, and the gravity acceleration $g = 9.8\ m/s^2$. In this paper, as the research was conducted in Guilin, Guangxi, the gravity acceleration is 9.7877 m/s^2, and the ideal value is 0.999 g.

In practical applications, due to the influence of various factors such as the thermoelectric effect, when the MEMS sensor is in a stationary state and the Z axis is perpendicular to the horizontal plane, the actual output value is not equal to the ideal value, that is, there is a zerobias error [27]. The existence of zero-bias error makes the initial displacement of the integration non-vanishing, and the error will accumulate due to the integration. In this paper, the offline calibration method is used to calculate the bias error of the MEMS sensor [28]. The output frequency of the MEMS sensor data is set to be consistent with the frequency used in the test. The MEMS sensor is placed statically, and the Z-axis is perpendicular to the horizontal plane. The output value of the MEMS sensor during a period a_z is collected, and the arithmetic average value a_m is calculated. The ideal value a_t is subtracted from the arithmetic average value a_m, and the bias error of the MEMS sensor can be obtained, the bias error is expressed in Eq. (1).

$$a_{\text{error}} = a_m - a_t \tag{1}$$

where a_{error} is the zero-bias, a_m is the arithmetic mean of the measured value, a_t is the ideal value of a_z.

(2) Fitting polynomial extreme value elimination trend

Assuming the acceleration signal is $a(t)$, the velocity signal is shown in Eq. (2).

$$\mathrm{v(t)} = \int_0^{\mathrm{t}} a(\mathrm{t})\mathrm{dt} = \mathrm{v}'(\mathrm{t}) + \mathrm{v}_0 \tag{2}$$

Then the displacement is expressed in Eq. (3).

$$s(t) = \int_0^t v(t)dt = s'(t) + s_0 \tag{3}$$

where $v'(t)$ is the original function of $v(t)$ and v_0 is the initial velocity, $s'(t)$ is the original function of $s(t), s_0$ is the initial displacement.

In fact, due to the influence of zero drift and other factors, the source acceleration signals collected by MEMS sensors generally contain noise and DC components. The acceleration signal is described by Zhu et al. [29], as shown in Eq. (4).

$$a(t) = a'(t) + \varepsilon \tag{4}$$

Thus Eqs. (2) and (3) become Eqs. (5) and (6).

$$v(t) = \int_0^t a(t)dt = v'(t) + (\varepsilon t + \delta) + v_0 \tag{5}$$

$$s(t) = \int_0^t v(t)dt = s'(t) + \left[\frac{1}{2}\varepsilon t^2 + (\delta + v_0)\, t + \eta\right] + s_0 \tag{6}$$

In the formula, δ and η are the integral constants generated after the first and second integration, respectively.

Due to the existence of a small DC component ε, the velocity signal obtained by integration contains a trend term, as expressed in Eq. (7)

$$\varepsilon t + (\delta + v_0) \tag{7}$$

Similarly, the displacement signal obtained by quadratic integration contains a quadratic trend term in Eq. (8).

$$\varepsilon t^2/2 + (\delta + v_0)\, t + (\eta + s_0) \tag{8}$$

Therefore, the polynomial of the source acceleration signal should be fitted before the integration to eliminate the trend term error caused by the presence of small DC components ε. The least squares method is the most commonly used method to eliminate the trend term.

Assuming that the source acceleration signal is $\{a_k\}$ $(k = 1, 2, 3, \ldots, n)$, fitting m-degree polynomials, as expressed inEq. (9).

$$\begin{gathered} x_m = b_0 + b_1 x + b_2 x^2 + \ldots + b_m x^m \\ (m = 1, 2, 3, \ldots, n) \end{gathered} \tag{9}$$

The polynomial expression of acceleration, using the undetermined coefficient method to determine the polynomial coefficient $b_j (j = 1, 2, 3, \ldots, m)$, so that the polynomial sum of squares of the difference value of the acceleration signal a_k and of error x_m minimum, expressed in Eq. (10).

$$\min E = \sum_{k=1}^{m} (x_m - a_k)^2 \tag{10}$$

In Eq. (10), the partial derivative of function E with respect to the variable b_j is obtained. If there exists an extreme value such that the partial derivative $\partial E/\partial b_j = 0$, then a system of linear equations of $(m + 1)$ elements is obtained. Solving the system of linear equations yields $(m + 1)$ undetermined coefficients $b_j (j = 1, 2, 3, \ldots, m)$ satisfying the condition.

2.2. Calculate displacement and velocity

The preprocessing of the acceleration signal first eliminates the effects of noise, zero drift, and DC component. The velocity and displacement signals are then solved, and the integral energy is determined. In this paper, velocity and displacement signals are solved using the Simpson rule [30].

$$\begin{gathered} v(t) = v(t-1) + \frac{a(t-1) + 4a(t) + a(t+1)}{6} \times \Delta t \\ (t = 0, 1, 2, \ldots, N-1) \end{gathered} \tag{11}$$

$$\begin{gathered} s(t) = s(t-1) + \frac{v(t-1) + 4v(t) + v(t+1)}{6} \times \Delta t \\ (t = 0, 1, 2, \ldots, N-1) \end{gathered} \tag{12}$$

In the formula, Δt is the sampling time, and the signal output is 0 when $t < 1$. The integral energy is expressed in Eq. (13).

$$v_{energy} = \sqrt{\sum_{t=0}^{N-1} v(t)^2} \tag{13}$$

where V_{energy} refers to the integral energy of velocity.

$$S_{energy} = \sqrt{\sum_{t=0}^{N-1} s(t)^2} \tag{14}$$

In Eq. (14), s_{energy} refers to the integral energy of displacement. The trending term is removed by the least square method, and the integral energy after removing the trend term is calculated again as shown in Eqs. (15) and (16), respectively.

$$v_{reenergy} = \sqrt{\sum_{t=0}^{N-1} v(t)^2} \tag{15}$$

In Eq. (15), $v_{reenergy}$ refers to the integral energy of velocity after removing trend term.

$$S_{reenergy} = \sqrt{\sum_{t=0}^{N-1} s(t)^2} \tag{16}$$

In Eq. (16), $s_{reenergy}$ refers to the integral energy of displacement after removing the trend term.

The energy loss that caused by detrending the velocity and displacement signals is compensated to obtain more accurate velocity and displacement signals based on Reference [31] and Eq. (17).

$$v_f(t) = \frac{v(t)}{v_{energy}\, v_{reenergy}} \tag{17}$$

In Eq. (17), $v_f(t)$ refers to the final velocity signal.

$$s_f(t) = \frac{s(t)}{s_{energy}\, s_{reenergy}} \tag{18}$$

In Eq. (18), $s_f(t)$ refers to the final displacement signal.

2.3. Algorithm Verification Based on Distance Test

(1) Experimental design

A fixed distance test based on a digital displacement sensor is designed to confirm the accuracy of algorithm. Fig. 2 depicts the test device. The displacement sensor module moves from left to right along the ruler, and MEMS sensors

fixed to the module gather and output the acceleration signal of the module movement while videotaping the module movement at each time corresponding to the displacement. The collected acceleration signal is combined with the related velocity and displacement data using the integration algorithm, and the timedisplacement coordinates of the module motion are then read from the video. In order to determine the relative error of algorithm and assess the test data error, the displacement from algorithm and video displacement are compared.

(2) Displacement from algorithm and relative error

Table 1 shows the relative inaccuracy of displacement and displacement computation for 30 groups of tests, and Fig. 3 shows the frequency distribution histogram of displacement from algorithms. The displacement from algorithms is primarily concentrated in the range of 990 mm to 1010 mm, accounting for about 46%. The minimum relative error of the displacement calculation is -0.11%, and the maximum is 3.86%.

One of the 30 groups of tests is chosen, and a curve depicting the progression of algorithm and video displacement over time is depicted in Fig. 4. In Table 2, the relative error of the displacement from algorithm calculation and the average relative error across the group of experiments are determined using 2 s as the time interval for comparing the video displacement corresponding to the displacement from algorithm of each movement.

It can be seen from Fig. 4 and Table 2 that the video displacement of this group is close to the displacement from algorithm. The relative error of the final displacement calculation of the algorithm is -1.26%, and the average relative error of the whole moving process is -6.28%.

(3) Error analysis of the test data

1. Test precision

   For the 30 set distance test results, the range R is,

   $$R = x_{\max} - x_{\min} = 1038.6 - 964.2 = 74.4$$

   The standard deviation is,

   $$s = \sqrt{\frac{\sum_{i=1}^{n} (x_i - \bar{x})^2}{n-1}} = 16.95$$

2. Outlier test

   The Grubbs test is used to test the algorithmic displacement data of the fixed distance test. The algorithmic displacements of 30 sets of fixed distance tests are shown in Table 1.

   The average value $\bar{x} = 1001.07$, the standard deviation $s = 16.95$, and the maximum deviation of the displacement (1038.6 mm) of the 24th test algorithm is $d_{p\max} = 37.5$ mm. Table $G_{(0.05,30)} = 2.745$, then $G_{(0.05,30)s} = 2.745 \times 16.95 = 46.53.37.5 = |d_{p\max}| < G_{(0.05,30)s} = 46.53$, so the 24th group of test displacement from algorithm (1038.6 mm) should be retained, and because other groups of displacement from algorithm deviation are less than $d_{p\max} = 37.53$, so the 30 groups of test displacement from algorithm data should be retained.

3. System error test

   Since the displacement data of 30 groups of test algorithms approximately obey normal distribution, ' t-test method ' can be used to test the systematic error of test results. 30 groups of test displacement from algorithm average $\bar{x} = 1001.07$, standard deviation $s = 16.95$, then $t = \frac{\bar{x}-\mu_0}{s}\sqrt{n} = \frac{(1001.07-1000)}{16.95} \times \sqrt{30} = 0.35$. The significance level $\alpha = 0.05$ and $df = 29, t_{0.05(29)} = 1.699$ and $t_{0.025(29)} = 2.045$ are expressed by the quantile of the t distribution. Because $0.35 = t < t_{0.025(29)} = 2.045$, there is no significant systematic error in the displacement calculation results of the algorithm.

3. Indoor model test of foundation pit

The indoor model test of foundation pit is designed to simulate the process of excavation. MEMS sensors are buried in the soil on the deformation side of the foundation pit to collect the acceleration signal of soil movement and the rotation angle of soil, so as to analyze the deformation characteristics of soil during excavation and verify the feasibility of applying MEMS technology to deformation monitoring.

3.1. Test model

This test simulates the foundation pit of the excavation without support. As shown in Fig. 5, the main body of the test model box is a frame structure welded by channel steel. Along the width direction of the model box, the front is 20 − mm thick transparent glass to observe the deformation of the soil in the box and the displacement of the supporting structure. The back and left and right sides are high-strength steel plates, and channel steel frame welding into a whole. The length, width, and height of the model box are 1.5 m, 0.6 m, and 1 m, respectively. Along the length direction, the model box is divided into two parts (0.9 m + 0.6 m) with a 20 mm thick high-density sawdust compression plate, and 0.9 m side is the deformation side, 0.6 m side is the excavation site of the foundation pit, and the high-density sawdust compression plate in the middle is used to simulate the support plate of the foundation pit.

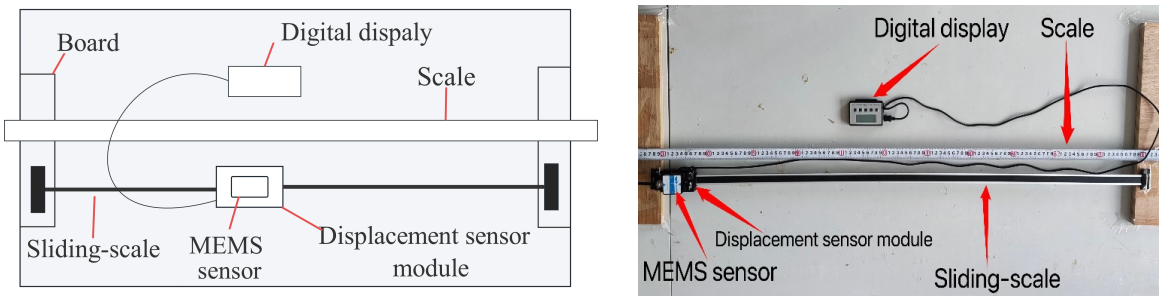

Fig. 2. Fixed distance testing device

Table 1. Experimental displacement from algorithm and relative error of 30 groups

Group	Displacement from algorithm/mm	Relative error/%	Group	Displacement from algorithm /mm	Relative error/%
1	986.2	-1.38	16	978.5	-2.15
2	1005.3	0.53	17	994.8	-0.52
3	996.2	-0.38	18	987.4	-1.26
4	998.9	-0.11	19	986.5	-1.35
5	1006.9	0.69	20	1020.5	2.05
6	1006.6	0.66	21	1033.6	3.36
7	998.3	-0.17	22	982.5	-1.75
8	1003.2	0.32	23	1025.4	2.54
9	1011.3	1.13	24	1038.6	3.86
10	1006.5	0.65	25	1011.1	1.11
11	995.5	-0.45	26	976.8	-2.32
12	1005.6	0.56	27	995.6	-0.44
13	964.2	-3.58	28	1018.9	1.89
14	1003.4	0.34	29	979.9	-2.01
15	998.2	-0.18	30	1015.6	1.56

Table 2. Comparison of video displacement and displacement from algorithm in group 11

Time /s	Video displacement /mm	Displacement from algorithm /mm	Relate error /%	Mean relative deviation/%
0	0	0	0	
2	56	49.5	-11.61	
4	196	175.6	-10.41	
6	321	296.4	-7.66	
8	443	408.1	-7.88	-6.28
10	582	530.7	-8.81	
12	708	644.7	-8.94	
14	786	756.8	-3.72	
16	897	853.1	-4.89	
18	982	944.1	-3.85	
19	1000	907.4	-1.26	

Through the transparent glass, the deformation of the soil on the deformed side of the box and the displacement of the support plate can be observed directly.

3.2. Test sand

The soil used in the model box of the test excavation is treated Guilin Li River sand, which is taken from the flood-plain section of the Darong River in the upper reaches of Li River. The collected Lijiang River sand is naturally dried and dried indoors, and then sieved with a 2 mm sand sieve. The basic physical and mechanical indexes of sand are shown in Table 3, and the particle gradation curve of the test sand is drawn by screening analysis as shown in Fig. 6. According to the curve results, the uneven coefficient of

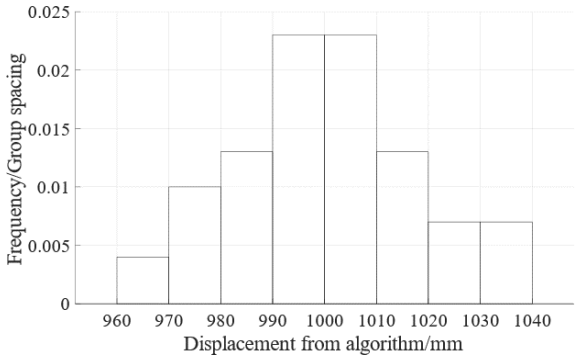

Fig. 3. Histogram of displacement from algorithm frequency distribution

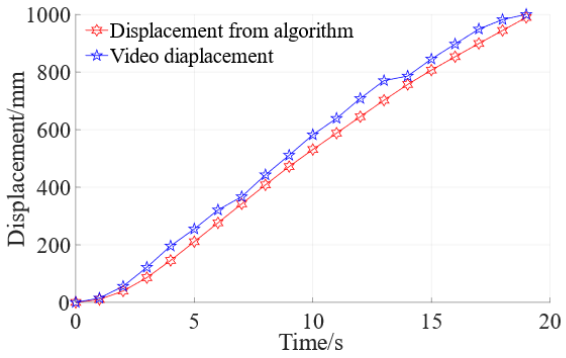

Fig. 4. Video displacement and displacement from algorithm curve- Group 11

soil Cu $= 3.75$, curvature coefficient $Cc = 0.15$

3.3. Monitoring device

The model of monitoring sensors used in the test are WT901B MEMS sensors and electromechanical dial indicators. A high-performance microprocessor is included with the WT901B MEMS sensor used in the test, which includes a high-precision gyroscope, accelerometer, geomagnetic field sensor, and powerful dynamic attitude solver. With the Kalman filter technique, it can precisely output the real-time motion in a dynamic environment. The sensor data output frequency is 0.2 Hz − 200 Hz0.2 Hz is selected in this test), the static measurement accuracy is 0.05°, and the dynamic measurement accuracy is 0.1°. Therefore, the acceleration value can be effectively recorded even at a lower excavation speed.

To send signals, the MEMS sensor and the electro-mechanical dial indicator are attached to the computer. The electro-mechanical dial indicator is fixed at a magnetic suction seat in a horizontal position. It is positioned in a specific location on the excavation side to monitor the horizontal displacement of the support plate specific position when the excavation depth increases. For the purpose of gathering the signal of soil movement, the MEMS sensors are layered in the deformation side of the model box. The electro-mechanical dial gauge utilized in the test has a precision of 0.01 mm and a range of 50 mm. The static strain gauge sends the horizontal displacement of support plate to computer.

3.4. Test monitoring scheme

(1) Layout of the MEMS sensors

The indoor model test simulated the process of excavation of the foundation pit. During the test, soil excavation was done by testers using shovel on the excavation side, and the placement of MEMS sensors was also conducted manually. This indoor model test does not yet correspond to a real excavation project, mainly to verify the feasibility of MEMS application in displacement monitoring.

As shown in Fig. 7(a), in order to better collect the acceleration signal of soil movement during the excavation, three layers of sensors are uniformly arranged from bottom to top along the depth of soil. According to the buried depth, from small to large, the three layers of sensors are referred to as first layer sensors, second layer sensors, and third layer sensors. The layout depth of the first layer sensor is 200 mm, the layout depth of second layer sensor is 400 mm, and the layout depth of third layer sensor is 600 mm. Each layer of the test is equipped with four sensors, as illustrated in Fig. 7(b), with the first layer of the sensor being denoted as from M9 to M12, the second layer as from M5 to M8, and the third layer as from M1 to M4.

In order to better collect the soil movement in the process of excavation, according to the numbering of the sensors, the first three numbered sensors of each layer are arranged along the middle line of the soil on the deformation side. For example, M9, M5, and M1 are placed along the plate, and the other two sensors of each layer are arranged at 100 mm intervals. A reference sensor is arranged for M9, M5, and M1 in each layer, and placed along the plate, which is 100 mm away from the center line of the soil on the deformation side, corresponding to M12, M8, and M4 for the three layers. It is necessary to measure the displacement of each point and fully perceive the displacement status of each point to reflect the deformation during the excavation, so if more sensors were applied, the more accurate the measurement results will be.

(2) Install electro-mechanical dial indicator

The purpose of installing an electro-mechanical dial indicator is to compare the displacement from algorithm with the measured displacement of the dial indicator, so as to

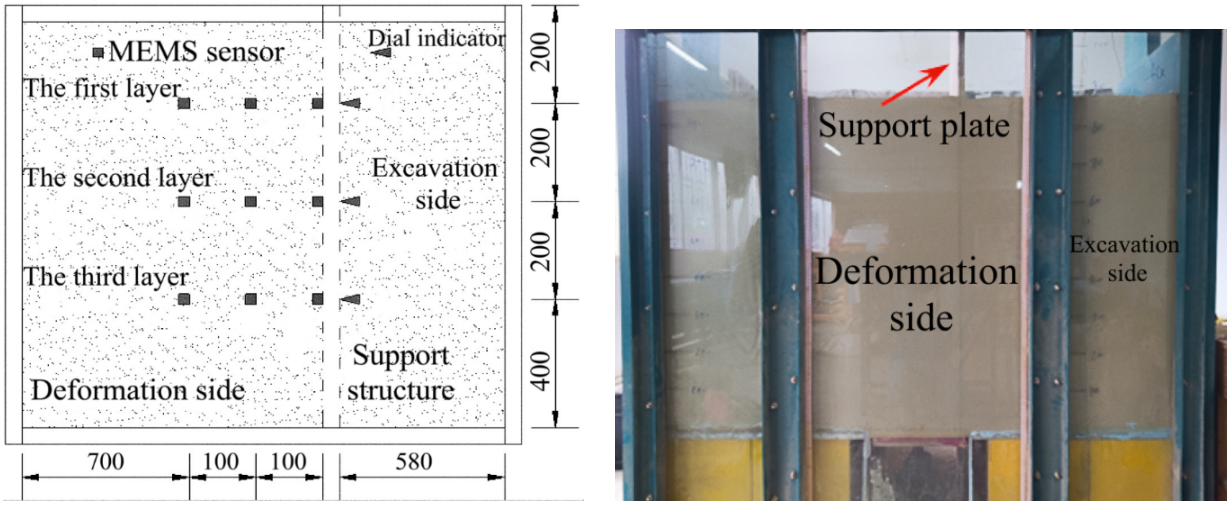

Fig. 5. Front view of model box

Table 3. Physical properties of test sand sample

Density /g · cm^{-3}	The angle of internal friction/	Cohesion /kPa	Static gravity	Water content /%
1.61	32.8	0.2	2.63	1.03

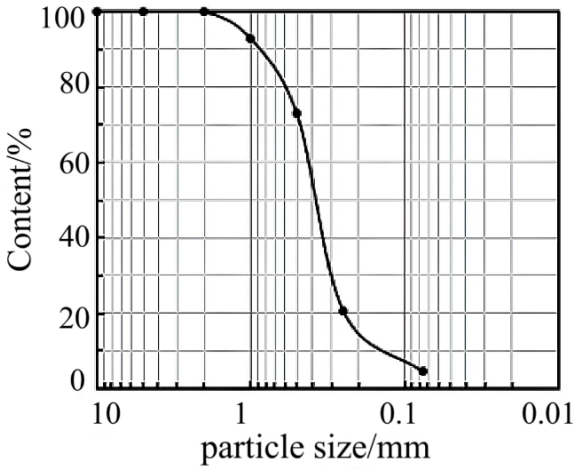

Fig. 6. Grain grading curve of test sand

verify the reliability and accuracy of the algorithm. Therefore, the installation of a dial indicator should meet the requirements of equivalent comparison in this test. On the middle line of the excavation side support plate of the foundation pit, an electro-mechanical dial indicator is installed horizontally at depths of 0.2 m, 0.4 m, and 0.6 m, respectively. According to the depth from small to large, it is denoted as B1, B2, and B3, respectively. Since the dial indicators of B1, B2, and B3 are only separated from M9, M5, and M1 by the supporting plate, the displacements measured by M9, M5, and M1 are theoretically equal to the displacements measured by B1, B2, and B3 dial indicators. In the simulation of excavation, when the depth of the excavation exceeds the depth of each layer of sensors, then install the corresponding dial indicators for each layer. During the actual test, the dial indicator B1 corresponding to M9 is installed at the depth of 0.25 m, the dial indicator B2 corresponding to M5 is installed at the depth of 0.4 m, and the dial indicators B1 corresponding to M9 is installed at the depth of 0.2 m, the excavation will continue until the foundation pit is 0.65 m. The dial indicator B3 corresponding to M1 is installed at the depth of 0.6 m. At 330 s, 590 s, and 840 s, the displacement compensation of B1, B2 and B3 is carried out according to the measured values of M9, M5, and M1 at the same position, so that the displacement measured by M9, M5, and M1 is approximately equal to the displacement measured by B1, B2, and B3 dial indicator.

3.5. Test procedures

(1) Connect the electro-mechanical dial indication and MEMS sensors, then number the devices.

(2) Fill and lay MEMS sensors

The high-density sawdust compression plate of the supporting structure is perpendicular to the glass surface and is erected at the boundary of the model box. The third layer of MEMS sensors is arranged in accordance with the sensor plane layout shown in Fig. 7(b), and both sides of the model

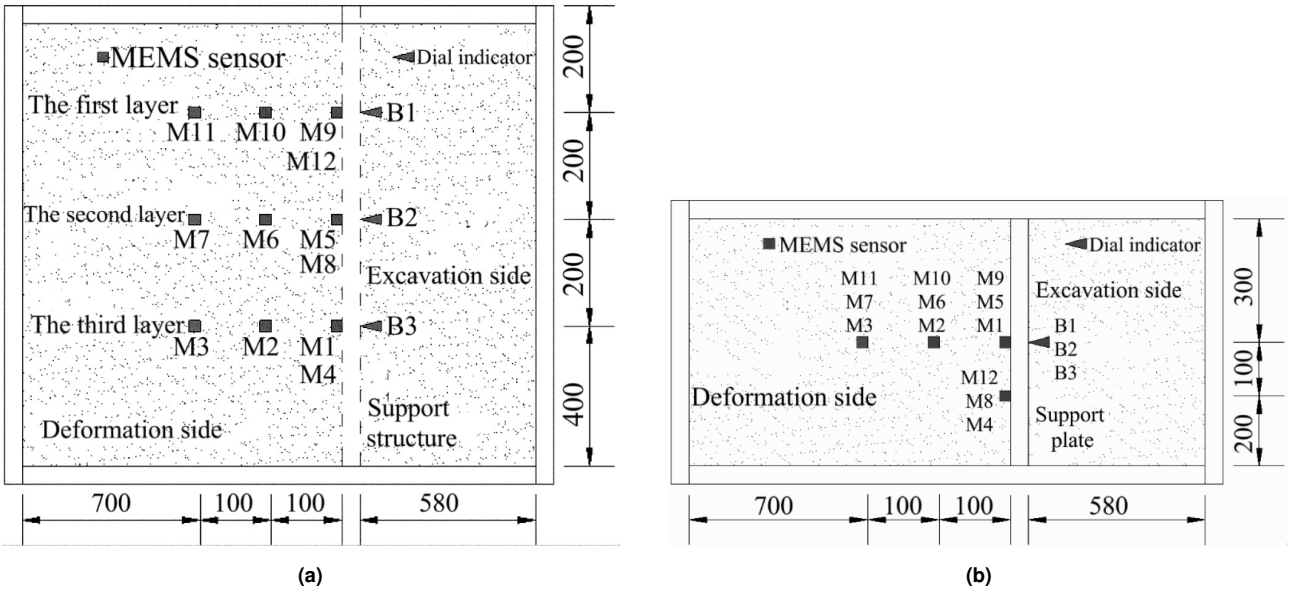

Fig. 7. Sensor layout diagram (unit /mm).

box are then filled evenly with a second layer of MEMS sensors up to a height of 0.6 m. The left and right sides of the model box are then filled with soil evenly to a height of 0.4 m. The initial layer of MEMS sensors was installed after the soil was continually filled to 0.8 m high on both sides of the model box. Fill the soil up to a height of 1 m, then stop filling, compact, and level the soil as necessary.

(3) Sensors debugging

According to the sensor number, the computer verifies each sensor is functioning normally. The host computer set the angle and acceleration to zeros before starting to record data and setting the sensor output at a frequency of 0.2 Hz.

(4) Simulate the excavation and install the dial indicator

The electro-mechanical dial indicator of this test is installed in the process of excavation. The excavation site of the foundation pit is excavated manually at a constant speed, and the excavation start time is recorded. When excavating to the depth of 0.25 m, install the B1 dial indicator on the supporting plate at the depth of 0.2 m, continue to excavate at the original speed, then the excavation depth is 0.45 m, and the B2 dial indicator is installed at the depth of 0.4 m along the middle line of the support plate. Continue with the original speed of uniform excavation, excavate to the depth of 0.65 m, install B3 dial indicator along the middle line of the supporting plate, continue to excavate at a constant speed until the excavation depth reaches 0.7 m and stop excavation.

(5) Save and arrange the test data

The foundation pit of the excavation in this test adopts a uniform and uninterrupted excavation method. The foundation pit of the excavation and the installation of the dial indicator are carried out independently without affecting each other. Finally, the total excavation depth of the excavation is 0.7 m, the total excavation time is 900 s, and the average excavation speed is about 0.78 mm/s.

4. Test results and analysis

Based on the above-mentioned MEMS acceleration signal transfer displacement algorithm, the acceleration signal of MEMS source collected in the model test is obtained, and the horizontal and vertical displacement of the soil during the excavation process is obtained, the displacement and rotation angle of the soil are used to analyze the deformation characteristics of the soil during excavation.

4.1. Horizontal displacement

Fig. 8 shows the comparison curves between the horizontal displacements of the M1, M5, M9 algorithms and the measured horizontal displacement of the corresponding dial indicators, as well as the curve of the excavation depth with time. In the model test, the measured displacement is labeled as dial indicator shown in the figures, and the algorithmic from displacement is representing the displacement calculated by the sensor data. It can be seen that the curve of the excavation depth with time is a straight inclining line. The total excavation depth of the foundation pit is 700 mm.

From Fig. 8, the corresponding dial indicators B1, B2 and B3, begin to show monitoring data from the time of 330 s, 590 s, and 840 s respectively, the displacement of B1,

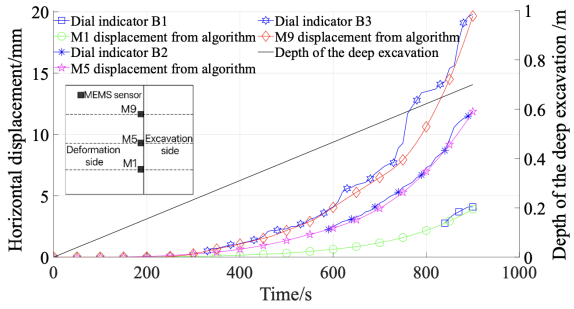

Fig. 8. Comparison between horizontal displacement measured by M1, M5, and M9, and dial indicator

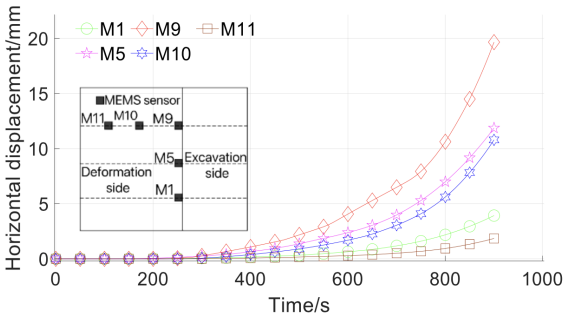

Fig. 9. Comparison of horizontal displacement of M1, M5, M9, M10 and M11 algorithms

B2, and B3 at these three times increases from zero, and at the corresponding time, the sensors M9, M5, and M1 have produced displacement. Therefore, in order to compare the displacement from algorithm and the displacement of the dial indicator (measured displacement), the displacement by B1 plus that by M9 at 330s (i.e. 0.5044 mm), the displacement by B2 plus that by M5 at 590s (i.e. 2.268 mm), and the displacement by B3 plus that by M1 at 840 s (i.e. 2.777 mm) are made, so that the displacement of the dial indicator and the corresponding displacement from algorithm start to change at the same starting point to facilitate comparison and analysis.

For M1, M5 and M9, the points are taken at a certain time interval respectively, and the relative errors of horizontal displacement corresponding to each point are calculated, as shown in Table 4. The average relative error of the displacement calculation of the three sensors during that period of the dial indicator is 10.6%, 10.1%, 9.5%, respectively. The relative error of the maximum horizontal displacement is 2.7%, 2.7%, and 2.2%, respectively. It can be seen that the relative error of the average horizontal displacement is less than 11%, and the relative error of the maximum horizontal displacement of the three sensors is less than 3%.

The displacement of the M1, M5, and M9 algorithms are smaller than the displacement measured by the dial indicator, that is because the signal energy compensation is insufficient during the acceleration signal integration, resulting in that the displacement calculated by the algorithm is slightly smaller than the actual monitored displacement.

Fig. 9 shows the curves of horizontal displacement of M1, M5, M9, M10, and M11 algorithms with time. According to the calculation, the maximum horizontal displacements of M1, M5, M9, M10, and M11 are 4.01 mm, 11.58 mm, 19.26 mm, 10.8 mm, and 1.85 mm, respectively. It can be seen that the horizontal displacement of the soil on the deformation side increases with the decrease of the soil depth during the excavation. The maximum horizontal displacement appears on the surface, and it also increases with the decrease of the distance from the supporting plate. The soil at the supporting plate has the maximum horizontal displacement according to reference [32]. The variation is consistent with the horizontal deformation characteristics of excavation obtained from the existing research literature, which also verifies the monitoring scheme and displacement calculation method in this paper, so it shows that the horizontal deformation of the soil at the top of the supporting plate should be monitored in practical engineering.

Fig. 10 show the curves of the horizontal displacement of the M1, M4, M5, M8, M9, and M12 algorithms with time. According to the deformation characteristics of the soil when the foundation pit has been excavated and combined with the location of M1, M4, M5, M8, M9, and M12, the horizontal displacement of the foundation pit has been calculated, theoretically, M1, M5 and M9 have equal horizontal displacements compared to M4, M8, and M12, respectively, the maximum horizontal displacements of M1, M4, M5, M8, M9, and M12 are 4.01 mm, 3.63 mm, 11.58 mm, 12.24 mm, 19.26 mm, 19.93 mm respectively. The difference in the maximum horizontal displacement between M1 and M4 is 0.38 mm, the proportion of the difference to the maximum horizontal displacement is 9.4% and 10.4% respectively, and the difference in the maximum horizontal displacement between M5 and M8 is 0.38 mm, the ratio of the difference to the maximum horizontal displacement was 5.7% and 5.4% respectively, and the difference of 0.67 mm between M9 and M12 was 3.5% and 3.4%, respectively. In theory, the difference in horizontal displacement between the two MEMS sensors with equal maximum horizontal displacement is less than 11% of their maximum horizontal displacement, which shows that the displacement calculation method used in this paper is stable, it is suitable for the calculation of soil

Table 4. Comparison between horizontal displacement measured by M1, M5, and M9, and dial indicat

Sensors	Time /s	Displacement from dial indicator/mm	Displacement from algorithm/mm	E_R /%	AARD /%
M1	850	3	2.84	-5.3	-9.6
	860	3.3	2.93	-11.2	
	870	3.5	3.11	-11.1	
	880	3.7	3.21	-13.2	
	890	3.9	3.34	-14.4	
	900	4.1	4.01	-2.2	
M5	650	3.3	3.05	-7.8	-10.1
	700	4.4	3.98	-9.5	
	750	5.7	5.29	-7.2	
	800	7.3	6.02	-17.5	
	850	9.6	8.11	-15.6	
	900	11.9	11.58	-2.7	
M9	400	1.1	1.07	-2.7	-10.6
	500	2.3	2.27	-1.3	
	600	4.1	3.46	-15.6	
	700	7.1	5.59	-21.3	
	800	13.5	10.83	-19.8	
	900	19.8	19.26	-2.7	

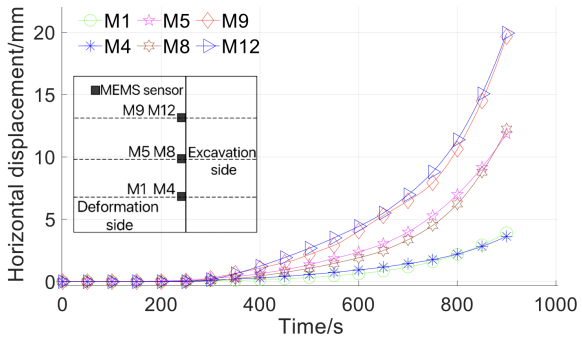

Fig. 10. Comparison of horizontal displacement of M1, M4, M5, M8, M9 and M12

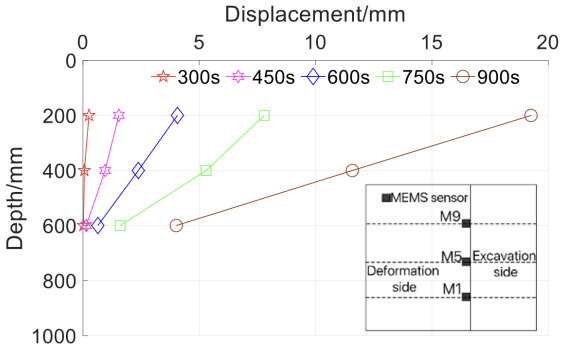

Fig. 11. The horizontal displacement from algorithm at different time points M1, M5 and M9

deformation and displacement during the excavation.

Fig. 11 shows the horizontal displacement curves of M1, M5, and M9 at 300s, 450s, 600 s, 750s, and 900s, respectively. As it can be seen from Fig. 11, as the excavation progresses, the horizontal displacement of the three sensors (i.e. M1, M5, and M9) increases gradually, and the horizontal displacement of the sensors decreases with the depth of the sensors gradually which is consistent with the variation described by reference. When the excavation is 900 s, the excavation depth is 700 mm. The excavation depth exceeds the buried depth of all sensors. It can be seen that the maximum horizontal displacement of the three sensors of M1, M5, and M9 is approximately linear which is consistent with reference. Among them, the maximum horizontal displacement from M9 is 19.26 mm, followed by the horizontal displacement from M5, which is 11.58 mm, and the minimum horizontal displacement from M1 is 4.01 mm.

4.2. Vertical displacement

The vertical displacement curves of the M1, M5, M9, M10, and M11 algorithms are shown in Fig. 12. The maximum vertical displacement of the five sensors are 0.78 mm, 6.11 mm, 15 mm, 8.02 mm, and 1.27 mm, respectively. Thus it can be seen the vertical displacement of the deformed soil increases with the decrease of the soil depth, and the maximum vertical displacement is found at the surface, With the decrease of the relative distance between the support plate and sensors, the soil at the support has the maximum vertical displacement, which is consistent with the variation of displacement described by reference.

M1, M5, and M9 are distributed equally along the ver-

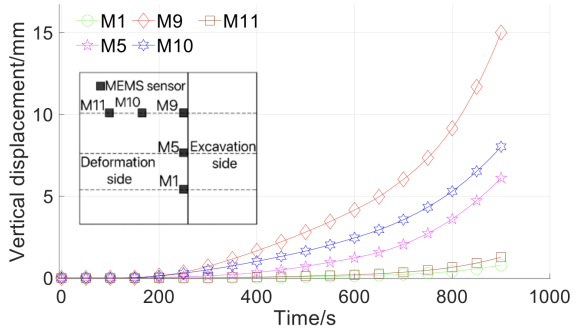

Fig. 12. Comparison of vertical displacement of M1, M5, M9, M10 and M11 algorithms

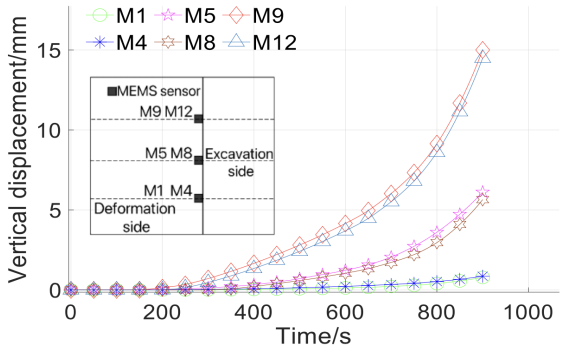

Fig. 13. Comparison of vertical displacement of M1, M4, M5, M8, M9 and M12 algorithms

tical direction, and the distance is 200 mm vertically. As the vertical displacement between M1 and M5 increases by 5.33 mm, and the average vertical displacement per mm of depth increases by 0.027 mm, the vertical displacement between M5 and M9 increases by 8.89 mm, and the average vertical displacement per mm of depth increases by 0.044 mm. Therefore, the closer to the surface, the faster the vertical displacement increases. M9, M10, and M11 were evenly distributed along the horizontal direction. The distance between M11 and M10 was 100 mm, and the vertical displacement between M11 and M10 increased by 6.75 mm and 0.068 mm respectively, the vertical displacement between M10 and M9 increases by 6.98 mm, and the average vertical displacement per mm distance increased by 0.07 mm. It can be seen that the closer of the sensors approaches to the support plate is, the faster the vertical displacement increases.

As seen in Figs. 9 and 11, the slope at the end of the displacement curve is not zero for both horizontal and vertical displacements, because in the present model test, when the excavation time reaches 900 s, the excavation approaches to failures, so the slope of the excavation curve is not zero as the velocity of the soil is not zero.

Fig. 13 shows the curves of time-vertical displacements of the M1, M4, M5, M8, M9, and M12 using algorithms. Theoretically, M1, M5, and M9 have the same vertical displacements as M4, M8, and M12, respectively, the maximum vertical displacements of M1, M4, M5, M8, M9, M12 is 0.78 mm, 0.86 mm, 6.11 mm, 5.64 mm, 15 mm, 14.49 mm, respectively. The maximum vertical displacement between M1 and M4 is 0.08 mm and the proportion of the difference to the maximum vertical displacement is 10.3% and 9.3% respectively, the difference in the maximum vertical displacement between M5 and M8 is 0.47 mm, and the proportion of the difference to each maximum vertical displacement is 7.7% and 8.3% respectively, the difference in the maximum vertical displacement between M9 and M12 is 0.51 mm, the difference accounted for 3.4% and 3.5% of each maximum vertical displacement, respectively. The difference of vertical displacement between the two MEMS sensors whose maximum vertical displacement is equal in theory is less than 11% of their maximum vertical displacement, which shows that the displacement calculation method or integration algorithm used in this paper has good stability and is suitable for the displacement calculation of soil deformation during the excavation of foundation pit in this test.

Fig. 14 shows the vertical displacement from algorithm at 300s, 450s, 600s, 750s, and 900s for M9, M10, and M11, respectively, the vertical displacement of M9, M10, and M11 gradually increases, and the maximum excavation depth reaches 700mm at the time of 900s, at this time, the maximum vertical displacements of M9, M10, and M11 are 15 mm, 8.02 mm and 1.27 mm, respectively. The closer to the support plate, the faster the vertical displacement increases. At the same excavation time, the closer of the sensors to the support plate, the greater the vertical displacement, which has been stated by reference.

4.3. Analysis of soil rotation angle

During the excavation in the model test, the deforming soil mainly rotates along the Yaxis of the MEMS sensor. Fig. 15 shows the curves of the rotation angles of M1, M5, M9, M10, and M11 with time. According to the location of the sensor, it is found that the rotation angle of the deforming soil increases gradually with the decrease of the soil depth, and the surface soil has the maximum rotation angle. With the decrease of the distance to the support plate, the changing trend is gradually increasing, in which the soil at the support plate has the maximum rotation angle. The reverse rotation of M10 occurred during time from 240 s $\sim$ 510 s,

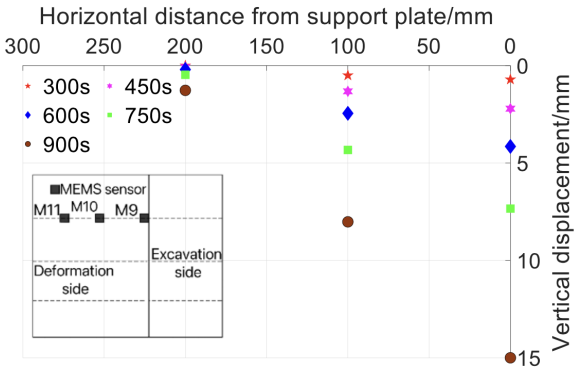

Fig. 14. The vertical displacement from algorithm at different time points M9, M10 and M11

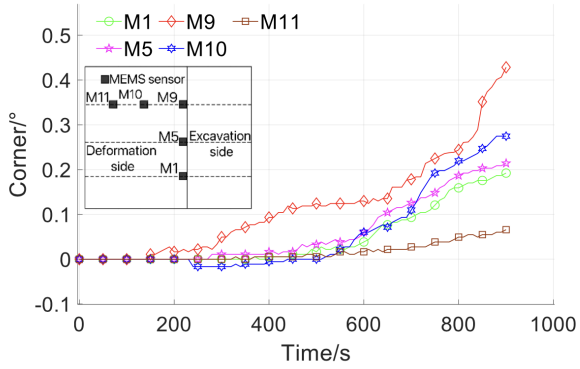

Fig. 15. Corner curves of M1, M5, M9, M10 and M11

which may be due to soil uneven deformation caused by the reverse rotation of M10 soil.

On the whole, in the unsupported excavation, the horizontal displacement of soil increases with the decrease of soil depth, and the maximum horizontal displacement appears at the ground surface. The vertical displacement (i.e. settlement) of soil also increases with the decrease of the distance from the supporting plate, in which the soil surrounding the supporting plate has the maximum vertical displacement, and the closer of the sensors the distance from the supporting plate, the faster the vertical displacement rate of soil increases. The deformation reflected by the corner signal are basically consistent with those reflected by the displacement signal.

Based on the research above, the MEMS sensor has the advantages of high precision and small size, so it can be easily placed in different depths and positions of the excavation to form effective monitoring and has the advantage of real-time data acquisition. Therefore, the MEMS sensor measurement technology can be used as an effective supplement to the traditional deformation monitoring method of the excavation. In the indoor model tests, the MEMS sensors were able to monitor the soil displacement. However, this test was not able to simulate a real pit excavation project. More tests are needed to verify the feasibility of MEMS sensors in real foundation pits.

5. Conclusions

This research examines the use of MEMS technology for monitoring foundation pit deformation. First, a time domain integration-based acceleration signal to displacement technique is proposed. A fixed distance test is used to confirm the accuracy and correctness of the algorithm. The foundation pit deformation monitoring interior model test is then completed. The MEMS sensor is buried in the soil to collect the acceleration and rotation angle signals of the soil deformation motion, and then the acceleration signal is converted into the corresponding displacement signal by algorithm integration. Finally, the soil displacement and rotation angle signals are used to analyze the deformation characteristics of the soil during excavation. The feasibility of applying MEMS technology to foundation pit deformation monitoring is explored. The following conclusions are drawn.

(1) MEMS technology can be used to monitor the deformation of deeply buried soil in a foundation pit. The monitoring method can achieve monitoring of soil deformation throughout the excavation without relying on zero displacement reference points. When excavating the foundation pit, the resulting rotation angle signal and the displacement signal calculated by the algorithm accurately reflect the soil deformation characteristics and have a positive monitoring impact.

(2) The algorithm is stable and suitable for the calculation of soil displacement when MEMS sensors are used to monitor the deformation of foundation pit soil. The relative error of the maximum horizontal displacement is less than 3% and the average relative error is less than 11% when the acceleration signal displacement algorithm based on time domain integration is applied to the data from indoor model test of foundation pit.

Acknowledgments

This work was Supported by the Opening Project of Sichuan Province University Key Laboratory of Bridge Non-destruction Detecting and Engineering Computing (No. 2023QYY01).

References

[1] R. A. Mangushev, A. I. Osokin, and L. V. Garnyk, (2016) *"Experience in preserving adjacent buildings during excavation of large foundation pits under conditions of dense development"* **Soil Mechanics & Foundation Engineering *53***(5): 291–297. DOI: 10.1007/s11204-016-9401-9.

[2] P. Lin, P. Liu, G. Ankit, and Y. J. Singh, (2021) *"Deformation monitoring analysis and numerical simulation in a deep foundation pit"* **Soil Mechanics and Foundation Engineering *58***(1): 56–62. DOI: 10.1007/s11204-021-09706-2.

[3] K. Ganjalipour, (2021) *"Review of inclinometer errors and provide correction methods for bias shift error and depth position error of the probe"* **Geotechnical and Geological Engineering *39***(6): 4017–4034. DOI: 10.1007/s10706-021-01743-w.

[4] E. S. Okiemute, M. N. Ono, and O. F. Oduyebo, (2018) *"Comparative analysis of DGPS and total station accuracies for static deformation monitoring of engineering structures"* **Journal of Environmental Science, Toxicology and Food Technology *12***(6): 19–29.

[5] J. G. Zhou, H. J. Xiao, W. W. Jiang, W. F. Bai, and G. L. Liu, (2019) *"Automatic subway tunnel displacement monitoring using robotic total station"* **Measurement *2020***: 15. DOI: 10.1016/j.measurement.2019.107251.

[6] H. Zhang, S. Xu, and T. Lu. "GPS height application and gross error detection in foundation pit monitoring". In: *Geotechnical Aspects of Underground Construction in Soft Ground: Proceedings of the Sixth International Symposium (IS-Shanghai), Shanghai-China, April-2008 (Vol-20)*. 2008, 239–242.

[7] L. Hu, Y. Zhang, H. Zhang, and S. Tian, (2014) *"Security monitoring technology of foundation excavation horizontal displacement by rapid static GPS method"* **Construction Technology *43***(16): 56–58.

[8] Z. X. Liu and X. J. Zhang, (2013) *"Research on deformation monitoring on supporting structure of deep foundation pit engineering based on gps"* **Applied Mechanics and Materials *239-240***: 595–598. DOI: 10.4028/www.scientific.net/AMM.239-240.595.

[9] B. Wolfgang and M. Andreas. "Investigating laser scanner accuracy". In: *Proceedings of Xixth Cipa Symposium*. ***10***. 2003, 696–702.

[10] X. L. Deng and L. H. Li, (2017) *"Refined modeling of complex geological body based on three-dimensional laser scanning technique"* **Journal of Engineering Geology *25***(01): 209–214. DOI: 10.13544/j.cnki.jeg.2017.01.027.

[11] D. Han, G. Qin, Y. Zhou, D. Wang, and Y. Yang, (2019) *"Application of BIM and 3D laser scanning in foundation pit monitoring"* **Journal of Chongqing Jiaotong University (Natural Science) *38***(06): 72. DOI: 10.1016/j.autcon.2021.103706.

[12] R. Bernini, A. Minardo, and L. Zeni, (2011) *"Distributed sensing at centimeter-scale spatial resolution by BOFDA: Measurements and signal processing"* **IEEE Photonics Journal *4***(1): 48–56. DOI: 10.1109/JPHOT.2011.2179024.

[13] C. Zhu, K. Zhang, H. Cai, Z. Tao, B. An, M. He, and J. Liu, (2019) *"Combined application of optical fibers and CRLD bolts to monitor deformation of a pit-in-pit foundation"* **Advances in Civil Engineering *2019***(1): 1–16. DOI: 10.1155/2019/2572034.

[14] J. Wu, L. Peng, J. Li, X. Zhou, J. Zhong, C. Wang, and J. Sun, (2021) *"Rapid safety monitoring and analysis of foundation pit construction using unmanned aerial vehicle images"* **Automation in Construction *128***: 103706. DOI: 10.1016/j.autcon.2021.103706.

[15] L. Wang, X. Weng, Y. Li, B. Guan, Z. Yao, and Q. Bo, (2018) *"Study on the application of ultrasonic wave in foundation settlement monitoring"* **Geotechnical Testing Journal *42***(2): 365–384.

[16] L. L. Guan, S. H. Zhang, Y. H. Li, and P. Sun, (2015) *"Application of dense surface modeling technology in displacement monitoring of deep foundation pit"* **Yangtze River *46***(11): 76–79.

[17] S. Alatza, I. Papoutsis, D. Paradissis, C. Kontoes, and G. A. Papadopoulos, (2020) *"Multi-temporal in SAR analysis for monitoring ground deformation in Amorgos Island, Greece"* **Sensors *20***(2): 338. DOI: 10.3390/s20020338.

[18] L. Yang, T. Wu, and S. Kang, (2002) *"The microsensor technology using to identify the initiation time of impact induced elastic waves"* **Journal of Applied Science and Engineering *5***(3): 121–127. DOI: 10.6180/jase.2002.5.3.01.

[19] V. Bennett, T. Abdoun, and M. Barendse, (2015) *"Evaluation of soft clay field consolidation using MEMS-based in-place inclinometer-accelerometer array"* **Geotechnical Testing Journal *38***(3): 290–302.

[20] C. Li, S. W. Song, and J. Z. Sun, (2023) *"Application and simulation research of MEMS inertial sensor in reservoir bank slope deformation monitoring"* **Chinese Journal of Rock Mechanics and Engineering *42***(05): 1248–1258.

[21] D. W. Ha, J. M. Kim, and Y. Kim, (2018) *"Development and application of a wireless MEMS-based borehole inclinometer for automated measurement of ground movement"* **Automation in Construction *87***: 49–59. DOI: 10.1016/j.autcon.2017.12.011.

[22] M. Darrow and D. Jensen, (2014) *"Cold region applications for in-place inclinometers based on microelectromechanical systems technology: Four evaluation case studies"* **Transportation Research Record: Journal of the Transportation Research Board *2433***(1): 1–9. DOI: 10.3141/2433-01.

[23] T. Abdoun, P. Bennett, L. Danisch, and M. Barendse. "Real-time construction monitoring with a wireless shape-acceleration array system". In: *Geotechnical Special Publication*. ***17***. 09. 2008, 533–540. DOI: 10.1061/40972(311)67.

[24] M. Barzegar, S. Blanks, B. Sainsbury, and W. Timms, (2022) *"MEMS technology and applications in geotechnical monitoring: A review"* **Measurement Science and Technology *33***(5): 052001. DOI: 10.1088/1361-6501/ac4f00.

[25] S. Stiros, (2008) *"Errors in velocities and displacements deduced from accelerographs: An approach based on the theory of error propagation"* **Soil Dynamics and Earthquake Engineering *28***(5): 415–420. DOI: 10.1016/j.soildyn.2007.07.004.

[26] A. Brandt and R. Brincker, (2014) *"Integrating time signals in frequency domain – comparison with time domain integration"* **Measurement *58***: 511–519. DOI: 10.1016/j.measurement.2014.09.004.

[27] L. Zhu, Y. Fu, R. Chow, B. F. Spencer, J. W. Park, and K. Mechitov, (2018) *"Development of a high-sensitivity wireless accelerometer for structural health monitoring"* **Sensors *18***(1): 262. DOI: 10.3390/s18010262.

[28] C. Yang, D. W. Tao, Q. Ma, Q. C. Jie, and L. Y. Wang, (2019) *"Realization of strong earthquake data processing technology based on Matlab"* **seismological and geomagnetic observation and research *40***(03): 148–153.

[29] H. Zhu, K. Gao, Y. Xia, F. Gao, S. Weng, Y. Sun, and Q. Hu, (2020) *"Multi-rate data fusion for dynamic displacement measurement of beam-like supertall structures using acceleration and strain sensors"* **Structural Health Monitoring *19***(2): 520–536. DOI: 10.1177/1475921719857043.

[30] V. Vukmirica, I. Trajkovski, and N. Asanovic, (2012) *"Two methods for the determination of inertial sensor parameters"* **Scientific Technical Review *60***(3): 27–33.

[31] X. Cheng, T. Zhou, F. Sun K.and Yang, H. Xie, and S. Wang, (2019) *"Time/Frequency-domain integration method of vibration acceleration signal processed by wavelet denoising"* **Electric power and energy *40***(06): 633–637.

[32] P. Hsieh and C. Ou, (1999) *"Shape of ground surface settlement profiles caused by excavation"* **Canadian Geotechnical Journal *35***(6): 1004–1017. DOI: 10.1139/t98-056.